Lab on a Chip

PAPER

Cite this: *Lab Chip*, 2025, **25**, 3270

Droplet microfluidics-assisted fabrication of Fe-alginate microgels with complex morphology: effect of the composition of droplets†

Jie Chen,[a] Penghui Li,[a] Ran An,[a] Aishan Cai,[a] Kaiqi Wang,[a] Zheyu Zhang,[a] Tao Wang*[e] and Yuandu Hu *[abcd]

Although shape-controllable alginate-based microgels *via* droplet microfluidics have been widely investigated, studies have mostly focused on tuning the designs of microfluidic devices and parameters of the crosslinking media, and very little attention has been paid to studying the effect of droplets' compositions on the morphologies of the resulting microgels. In the present study, droplets of aqueous solutions of sodium alginate (SA) with different additives (*i.e.*, 10 wt% dextran, PEG, or glycerol) have been produced from microfluidics and collected in solutions with different concentrations of glycerol (0–70 wt%) and $FeCl_3$ (2–10 wt%). The effect of droplet compositions on the morphologies of resulting Fe-alginate microgels has been systematically investigated. The results showed that the morphologies of the microgels were remarkably influenced by the interactions between the droplets and the collecting solutions, leading to the formation of microgels with different shapes. Additionally, microgels prepared under specific conditions exhibited certain deformation patterns. For example, dimpled microgels with large cavities exhibited an increase in cavity size in collecting solutions with higher concentrations of glycerol and $FeCl_3$ (the value of d/D rose from 0.3 to 0.5, D and d represent the outer contour dimension and the cavity diameter of the microgel). Similarly, red blood cell-like microgels showed an increase in concavity depth as the concentrations of glycerol and $FeCl_3$ increased (the value of D/L rose from 1.7 to 3.7, D represents the horizontal length of the microgel, and L indicates the vertical depth of the concave). The dimple-like microgels were uniquely advantageous in terms of rapid and efficient payload release (up to 98% release in 5 hours, 16.68 μg of total release), significantly superior to the spherical microgels (82% release in 5 h, 12.54 μg of total release). These findings establish a framework for morphological engineering of microgels, offering promising opportunities for applications in payload delivery systems requiring rapid and controlled release profiles.

Received 25th December 2024,
Accepted 21st May 2025

DOI: 10.1039/d4lc01101e

rsc.li/loc

1. Introduction

Hydrogel microparticles have emerged as critical components in various fields, including drug delivery,[1–4] tissue engineering,[5–8] and environmental remediation,[9–11] due to their tunable size, shape, and material properties. Among these attributes, the morphology of hydrogel microparticles plays a crucial role in their functionality,[12] significantly influencing mechanical strength, surface characteristics, flow behavior, and substance exchange rates.[13,14] For instance, spherical microparticles have been widely used in biomedical diagnostics, controlled drug release, and cell encapsulation due to their simple preparation process, ease of scalable production, and uniform shape.[15–18] However, despite their high reproducibility and predictable behavior, their application exhibits significant limitations when it comes to meeting complex biological or functional requirements.[19,20]

In recent years, the demand for non-spherical hydrogel microparticles (NSHPs) has been steadily increasing due to their unique advantages over spherical microparticles.[21–24] NSHPs exhibit anisotropic properties, such as a higher surface-area-to-volume ratio, enhanced cell adhesion capabilities, and improved diffusion efficiency.[25,26] These characteristics make them particularly valuable for advanced biomedical applications.[27–29] Various methods have been

[a] *Department of Materials Science and Engineering, School of Physical Science and Engineering, Beijing Jiaotong University, Beijing 100044, China. E-mail: huyd@bjtu.edu.cn*
[b] *Hubei Provincial Key Laboratory of Green Materials for Light Industry, Hubei University of Technology, Wuhan 430068, China*
[c] *Guangdong Provincial Key Laboratory of Technique and Equipment for Macromolecular Advanced Manufacturing, South China University of Technology, Guangzhou 510641, China*
[d] *Key Laboratory of Advanced Materials of Ministry of Education, Department of Chemical Engineering Tsinghua University, Beijing 100084, China*
[e] *Metals and Chemistry Research Institute, China Academy of Railway Sciences Corporation Limited, Beijing, 100081, China*

† Electronic supplementary information (ESI) available. See DOI: https://doi.org/10.1039/d4lc01101e

developed for preparing NSHPs, including photolithography,[30] phase separation,[31,32] and self-assembly techniques.[33,34] However, compared to these approaches, microfluidic technology offers distinct advantages, such as high production efficiency, excellent monodispersity, and continuous operation.[35–37] As a result, the microfluidic preparation of hydrogel microparticles, such as alginate-based hydrogel microparticles, has been extensively reported, with significant progress achieved in controlling their size and shape.[38–40]

Traditional studies on microfluidic preparation of alginate-based hydrogels have primarily focused on tuning external field parameters or device-specific parameters, such as flow rates, channel geometry, and external crosslinking methods, to control the morphology of microgels.[41–43] However, few studies have explored the synergistic regulation of droplet composition and external crosslinking solution parameters, despite droplet composition having significant impacts on its rheological properties. These properties, in turn, influence droplet deformation and structural evolution under external shear forces.[44,45] Given the unique characteristic of the crosslinking reagent Fe^{3+}, such as charge transfer capability, *etc.*, Fe-alginate bulk hydrogels have received considerable attention.[46] However, only until recently have Fe-alginate microgels with controllable morphologies been reported by varying the compositions of external collecting solutions.[47] The synergistic effect of droplet composition and external crosslinking parameters on the morphologies of the resultant microgels remains unclear. In particular, the effect of the addition of a Newtonian or non-Newtonian fluid composition into the alginate sodium solution on the rheological behavior of the droplet phase and then the resultant microgels' morphological evolution pattern still perplexes researchers. It is important to investigate the potential relationship given that uncovering this part could establish guidelines for future studies regarding the design of microgels with unconventional geometries. In this regard, this study investigated the effects of droplet composition, including additives, and their interaction with parameters of crosslinking solutions on the morphologies of Fe-alginate microgels.

This approach not only enabled the fabrication of non-spherical microgels with complex morphologies but also established a systematic method for controlling morphology. This breakthrough provided robust technical support for expanding the applications of hydrogel microparticles in payload delivery, tissue engineering, and environmental remediation.

2. Experimental section

2.1. Materials

Sodium alginate (SA, a: S875554, Macklin Biochemical Technology Co., Shanghai, China. b: W-201502, Sigma-Aldrich Trading Co. Ltd., Shanghai, China), poly(ethylene glycol) (PEG 6000, Sigma-Aldrich Trading Co. Ltd., Shanghai, China), glycerol ($C_3H_8O_3$, purity ≥ 99%, M_w = 92.09 Da, Innochem Science and Technology Co., Beijing, China), iron(III) chloride hexahydrate ($FeCl_3{\cdot}6H_2O$, purity ≥ 98.5%, M_w = 270.3 Da, Innochem Science and Technology Co., Beijing, China), Dextran 500 ($(C_6H_{10}O_5)_n$, M_w = 500 000 Da, Macklin Biochemical Technology Co., Shanghai, China), *n*-decyl alcohol ($C_{10}H_{22}O$, purity ≥ 98%, M_w = 158.28 Da, Macklin Biochemical Technology Co., Shanghai, China), Span 80 (Sigma-Aldrich). $Ru(bpy)_3Cl_2{\cdot}6H_2O$ (Energy Chemical, Saan Chemical Technology Co. Ltd, Shanghai, China). Technical pH Buffer solutions (pH 7.00 ± 0.02, Aladdin Biochemical Technology Co., Shanghai, China). Chitosan (CS, viscosity = 200 mPa s at 1 wt%, Innochem Science and Technology Co., Beijing, China), sodium tripolyphosphate ($Na_5P_3O_{10}$, purity ≥ 98%, M_w = 367.86 Da, Aladdin Biochemical Technology Co., Shanghai, China). Pure water was produced from a Mini-Q (Milli-Q Direct, Merck, Shanghai, China) ultrapure water production system.

2.2. Fabrication of the droplet dipping device

To fabricate a microfluidic device, a glass slide (25 × 76 mm), two cylindrical glass capillaries with tapered openings, and one square capillary are required. The cylindrical glass capillaries (100 mm in length, 0.5 mm inner diameter (I.D.), and 0.9 mm outer diameter (O.D.)) were heated and pulled to form tapered tips using a Narishige PC-10 micropipette puller. The tips were then polished with sandpaper to achieve suitable opening sizes, with the two tapered capillaries ground to ~45 μm and 300 μm, respectively. These capillaries were then inserted into the square capillary (1 mm I.D.), ensuring coaxial alignment with the distance between the tapered openings controlled at ~50 μm. The three capillaries were fixed onto the glass slide using resin, completing the basic assembly of the device.

The prepared microfluidic device was placed on the observation stage of an optical microscope. Two syringes, filled with the dispersed phase (DP) and continuous phase (CP) liquids, respectively, were mounted onto syringe pumps. Rubber tubing (O.D. = 0.5 mm, I.D. = 1.5 mm) was used to connect the syringes to the microfluidic device, and the flow rates of the syringe pumps were adjusted to control the flow of the DP and CP, allowing droplets to form within the device. At the outlet of the device, rubber tubing was attached to guide the generated droplets into a collection solution. The distance between the rubber tubing and the beaker containing the collection solution was adjustable *via* a lifting platform to ensure smooth droplet collection.

2.3. Production of SA droplets containing different additives and preparation of Fe-alginate microgels with different morphologies

In this experiment, three additives with different molecular weights (M_w) but the same mass fraction (10 wt%), dextran (M_w 500 000), PEG (M_w 6000), and glycerol, were added to a 2 wt% SA solution as the DP. Meanwhile, a solution of 5 wt% Span 80 surfactant in decanol was used as the CP. Span 80 was employed to reduce the interfacial tension between the DP and CP, thereby promoting the uniform generation of

droplets. The DP and CP (1 mL and 5 mL, respectively) were loaded into syringes and injected into the microfluidic device using syringe pumps. To produce monodisperse initial droplets with a size of ~200 μm, the flow rates of the CP and DP were set to ~1800 μL h^{-1} and ~50 μL h^{-1}, respectively. Due to the significant flow rate difference, the fast-moving CP generated a large shear force along its flow direction, which stretched and deformed the slower-moving DP. When the shear force exceeded the surface tension of the DP droplets, the dispersed liquid broke up into individual droplets under the traction of the CP, forming discrete droplets within the device. The droplet size primarily depended on the flow rate ratio of the CP to the DP. A higher CP flow rate produced greater shear forces, resulting in smaller droplets, while reducing the CP flow rate or increasing the DP flow rate yielded larger droplets. Thus, precise control of the flow rates allowed regulation of the droplet size and generation rate.

The initial droplets were then guided off the device *via* rubber tubing into a collection solution consisting of glycerol (0–70 wt%) and $FeCl_3$ (2–10 wt%). To control the dropping height of the droplets, the beaker containing the collection solution was placed on a lab lift stand platform, maintaining a fixed distance of 17.5 mm from the outlet of the rubber tubing. As the initial droplets exited the device, they were carried by the CP into the collection solution. Upon entering the solution, oil–water separation occurred due to differences in density and hydrophobicity. The CP spread rapidly on the surface of the collection solution, while the droplets came into contact with the Fe^{3+} in the collection solution and underwent crosslinking reactions. During the crosslinking process, the iron ions diffused into the droplets and interacted with the carboxyl groups in SA to form a stable gel network. The final morphologies of the gels were influenced by factors such as the composition of the droplets and collection solution, as well as the collecting height, resulting in diverse gel structures. This method not only ensured the morphological diversity of the droplets but also imparted high stability to the resulting gel networks.

2.4. Shear rate-viscosity test of droplets with different additives

We took 3 mL of SA solution containing one of the three components (dextran, PEG, or glycerol) and carefully loaded the samples into the rheometer's measurement area. Special attention was paid to avoid bubbles and it was ensured that the sample fully covered the measurement area. The temperature was set to 20 °C. The range and increment mode for the shear rate were set typically from a low shear rate and gradually increased to a high shear rate to capture the viscosity changes across the range. The rheometer was then started, recording the viscosity values of each sample at different shear rates. The rheometer automatically adjusted the shear rate and measured the corresponding viscosity. After the completion of the tests, data were exported to the Origin software for further analysis and optimization to obtain the shear rate–viscosity curves.

2.5. Fluorescence functionalization and characterization of microgels

First, the Fe-alginate microgels with different morphologies were thoroughly washed with distilled water to remove all residues of the collection solution, ensuring purification of the samples. The cleaned microgels were then observed using a microscope under both transmission and fluorescence modes to assess their initial color and morphology. Transmission mode provided detailed structural information of the microgels, while fluorescence mode confirmed whether the microgels exhibited any intrinsic fluorescence characteristics. Subsequently, the microgels were immersed in a solution of 0.5 wt% poly(*N*-isopropylacrylamide-*co*-$Ru(bpy)_3$) (pNIPAAm-*co*-$Ru(bpy)_3$) for 30 minutes to allow binding with the ruthenium-functionalized linear polymers. After soaking, the microgels were removed from the solution and thoroughly rinsed with DI water multiple times to ensure complete removal of any unbound polymers, preventing interference from surface-adhered, unbound polymers in subsequent observations. The cleaned microgels were gently transferred onto a clean glass slide using a dropper for microscopic observations. The microgels were observed using the microscope (Olympus BX 53 M, Olympus Corporation, Beijing, China) under both transmission and fluorescence modes to examine any changes in morphology and color, as well as to confirm successful acquisition of fluorescence characteristics. For stable fluorescence imaging, the exposure intensity was carefully controlled in fluorescence mode to avoid over- or underexposure that could compromise image quality. Throughout the experiment, the concentration of the polymer solution and immersion time were strictly controlled to ensure reproducibility and accuracy of results. These key parameters helped to achieve consistent binding between the microgels and the ruthenium-functionalized polymers, thereby reliably producing the desired fluorescence effects. This treatment and observation process provided reliable data support for subsequent studies of the optical properties of the microgels.

2.6. Characterization of microgels using optical microscopy and scanning electron microscopy (SEM)

In this experiment, an optical microscope (LWD 300–38 LT, Beijing Cewei Optoelectronics, Beijing, China) was used to observe the morphologies of the microgels, and images were captured using a high-speed CCD (20 MP, USB 3.0) connected to the microscope. The deformation process of the initial droplets in the collection solution was recorded using a Sanqitid optical 48 MP high-definition industrial electronic microscope (TDTZGX4KHU).

A droplet of an aqueous dispersion containing microgel particles was placed on a clean silicon wafer with conductive adhesive and pre-frozen in a refrigerator (KONKA-BCD-102S)

for 1 hour. The wafer was then removed and placed in a vacuum freeze-dryer (FHYQ202409Y) for ~3 hours of freeze-drying. The samples were coated with a 5 nm thick gold layer using a sputter coater (HIYACHI-MC1000), and their surface morphology was imaged with a scanning electron microscope (SEM, Thermo Fisher-Apreo C).

2.7. Cross-system validation using chitosan-TPP microgels

To verify the universality of this method, we also applied the strategy to prepare chitosan/tripolyphosphate (CS-TPP) microgels by using the droplet deformation at the interface. We used an aqueous solution containing 1 wt% chitosan (CS) and 1% acetic acid as the dispersed phase and *n*-decane solution of 5% Span 80 as the continuous phase. Droplets of the chitosan solution were introduced into a series of collection solutions containing both glycerol with varied concentrations (10–50 wt%) and TPP with different concentrations (2–6 wt%). The different concentrations of the two components were assumed to induce droplet deformation and further crosslinking reaction to form CS-TPP microgels. In addition, adding 0–50 wt% of glycerol to the chitosan solution-based dispersed phase can be also used to regulate the droplet's viscosity, and the droplets with different viscosities were subsequently crosslinked in collection solutions with a fixed TPP concentration (2 wt%). The morphological evolution of microgels in different glycerol concentrations, TPP concentrations, and droplet viscosities was systematically characterized.

2.8. Microgels' loading and release of model molecules

Given its fluorescence characteristics and positively charged nature in water, $Ru(bpy)_3Cl_2$ was selected as the model molecule (payload) to be loaded into the microgels by spontaneous diffusion. The positive charges of the molecules can form weak interactions with the carboxyl groups in the hydrogel skeleton. Two morphologies (spherical and dimpled) of Fe-alginate microgels were respectively immersed in 1 mg mL^{-1} solutions of this compound. The samples were incubated under gentle vibration at room temperature for 24 h to ensure sufficient payload loading. After removing unbounded free molecules *via* repeated DI water washing, the payload microgel samples (10 mg) were placed in 3 mL PBS buffer (pH = 7.00 ± 0.02) and subjected to payload release experiments under constant vibration. At pre-set time points, aliquots of the release medium were withdrawn, and the absorbance of $Ru(bpy)_3^{2+}$ was measured at λ_{max} = 454 nm using a UV-vis spectrophotometer (UV-2600). Payload concentrations were calculated based on the standard curve equation ($y = 0.0123x + 0.0047$, $R^2 = 0.9987$), and cumulative release rates were determined *via* a mass balance method to plot payload release kinetic curves. All absorbance values fell within the instrument's linear response range (Abs = 0.1–4.5), and relative standard deviations (RSD) of triplicate experiments were <5% (n = 3), confirming good reproducibility and reliability of the results.

2.9. Statistical analysis

All data were expressed as mean ± standard deviation (SD). The effects of glycerol and $FeCl_3$ concentrations on the morphologies (d/D and D/L values) of the resultant microgels were analyzed by one-way ANOVA with Tukey's post-hoc test for multiple comparisons. Statistical significance was defined as $p < 0.05$. All analyses were performed using GraphPad Prism 9.0 (GraphPad Software, USA).

3. Results and discussion

3.1. Effect of the disperse phase's composition on the formation of droplets and the tuning of microgel's morphologies

By precisely adjusting the flow rates of the continuous phase (CP) and dispersed phase (DP), a batch of uniform water-in-oil (W/O) droplets (composed of 2 wt% SA and 10 wt% dextran) was continuously generated in a microfluidic device (Fig. S1a and b†). The resultant droplets exhibited excellent monodispersity, and the average droplet size was approximately 223 μm. This indicated that the droplet generation process was highly controllable, although the DP is a characteristic non-Newtonian fluid (Fig. S1c†). In the experiment, the DP was composed of 2 wt% SA and one of three additives with different molecular weights but identical mass fractions (10 wt% dextran (M_w ~ 500 000), PEG (M_w ~ 6000), and glycerol (M_w ~ 92)). The addition of these additives led to the DP with different viscosities, which ranked as SA–dextran > SA–PEG > SA–glycerol, as shown in their shear rate–viscosity curves in Fig. S2.† Since different M_w of SA have an effect on the droplet sizes and rheological properties, we carried out a systematic characterization of two different molecular weights of SA, and the differences in molecular weight distributions were confirmed using gel permeation chromatography (GPC) (Fig. S3a and b†). Dynamic shear rheology tests (Fig. S3c†) showed that the zero-shear viscosity of the high M_w SA solution showed an obvious increase (from 2 mPa s to 14 mPa s). Fig. S3d† illustrated that the corresponding average droplet diameter increased from 210 μm to 228 μm at the same flow rate (DP = 70 μL h^{-1}, CP = 1200 μL h^{-1}). This was because the entanglement of the chains of high M_w SA was enhanced, and correspondingly the ability to resist shear force fracture was stronger. The relatively high viscosity of the high M_w SA solution was not conducive to ion diffusion and droplet deformation. Comparably, a relatively low viscosity of the low M_w SA solution made the droplets more deformable, which enabled a relatively faster crosslinking rate, which was conducive to the efficient regulation of the morphology of microgels.

In the microfluidic device, the DP was subjected to shear and stretching by the CP flow to generate droplets. The higher the viscosity of the DP, the more resistance to overcome. This was because a high-viscosity DP exhibited stronger cohesion, inhibiting droplets from deformation and fission. Under the same shear force, a higher viscosity DP required more time to split, accumulating more volume before splitting. As a result, the DP under this condition

tended to form larger droplets. For example, when the flow rates of the DP and CP were 50 μL h^{-1} and 1600 μL h^{-1}, the average droplet diameters ranked by viscosities of the DPs were 238, 229, and 220 μm, respectively. This phenomenon indicated that at the same flow rate, higher viscosity of DPs typically produced larger droplets (Fig. S1d†). Furthermore, smaller droplets were generally produced when the viscosity of the DP was kept constant but the CP's flow rate was increased. This was because a higher CP flow rate applied stronger shear force to the DP, stretching it into finer liquid threads that generated smaller droplets upon splitting. Additionally, the faster CP flow exerted greater compressive forces on the DP, further inhibiting the DP from aggregating. Under the combined effects of shear and compression forces, the DP was split into smaller volumes more rapidly, leading to a significant reduction in droplets' size. The results clearly demonstrated that a faster CP flow can effectively lead to a reduction in the droplets' size. These features were achieved in the microfluidic device by precisely controlling the flow rates of the CP and DP, as well as the viscosity of the DP, ensuring consistent droplet morphology and size throughout the production process.

When the droplets with different components were dropped from a fixed height of 17.5 mm into the $FeCl_3$ solutions with varying concentrations and viscosities, the droplets experienced different degrees of deformation due to the influence of multiple effects of the collection solution. In particular, the viscosity relationship and osmotic pressure values of the collection solutions are shown in Fig. S4 and Table S1 in the ESI.† The droplets with different compositions exhibited varying degrees of deformation due to differences in density and viscosity. Droplets with lower viscosities were prone to a greater deformation at the bottom part during the sedimentation process. Once the droplets came into contact with the collection solution, Fe^{3+} from the collecting solution rapidly diffused into the droplets and crosslinked with the carboxyl groups, leading to the formation of a network structure. This crosslinking reaction typically initiated at the droplet's outer layer and gradually progressed inward. The rate of crosslinking depended on the $FeCl_3$ concentration, with higher concentrations resulting in a faster crosslinking and more pronounced deformation of droplets. The viscosity of the $FeCl_3$ solution also influenced the droplet's deformation. In high-viscosity $FeCl_3$ solutions, the droplets encountered greater fluid and ion diffusion resistance, leading to a slower and more pronounced deformation. Therefore, when SA droplets of different compositions fell onto the collection solution from a fixed height, the resulting microgels exhibited various morphologies under the combined effects of possible impact force, ionic crosslinking rate, osmotic pressure differences, interfacial tension, and the external solution's viscosity (Fig. 1). Through the synergistic effect, SA droplets with different compositions resulted in the formation of microgels with specific shapes and structures, offering potential for diverse applications.

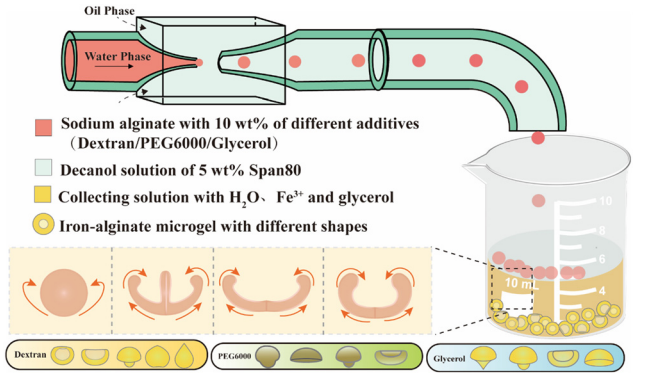

Fig. 1 A cartoon illustration showing the generation of initial water-in-oil droplets with different compositions in a microfluidic device, followed by an off-chip crosslinking process to obtain a series of Fe-alginate microgels with diverse morphologies and compositions.

3.2. Kinetic analysis of the droplet deformation mechanism

The deformation of droplets in the environment of the current case was mainly influenced by the comprehensive effects of shear force, surface tension, gravity, and crosslinking kinetics. Once the droplets were collected in the collection liquid, their deformation process can be divided into two stages: a possible impacting-induced deformation and a subsequent crosslinking induced deformation. At the first stage of possible impacting-induced deformation, the droplets were subjected to the action of inertial impact force and the resistance of the collection liquid. As a result, they underwent a temporary deformation due to hydrodynamic forces. The initial deformation rate of the droplets can be quantified by the Weber number (We)[48] and the Reynolds number (Re),[49] which are defined as below:

$$\mathrm{We} = \rho v^2 D/\gamma \quad (1)$$

$$\mathrm{Re} = \rho v D/\eta \quad (2)$$

where ρ is the density of the droplets, v is the incident velocity of the droplets, D is the diameter of the droplets, γ is the interfacial tension, and η is the viscosity. We summarized the We and Re values of the droplets in collection liquids with different compositions (Table 1). The results show that $\mathrm{We} \ll 1$ under all conditions, indicating that the interfacial tension dominated the stability of the droplets. The droplets tended to maintain their spherical shape when encountered with the external fluid. The interfacial tension measurement is shown in Fig. S5.† Under this circumstance, the inertial impact had a neglect effect on the morphological evolution. This enabled the droplets to maintain their integrity and form a stable and controllable microgel morphology under the action of external shear forces and crosslinking kinetics. The small Reynolds number ($\mathrm{Re} < 1$) suggested that the deformation process of the droplets was mainly controlled by the synergistic effect of viscous forces, surface tension, and cross-linking kinetics, rather than the inertial force. This also

Table 1 Weber numbers and Reynolds numbers for the droplets in collecting solutions with different concentrations of glycerol and $FeCl_3$

The concentration of glycerol (wt%)	0	10	30	50	70
The concentration of $FeCl_3$ (wt%)	2	4	6	8	10
We	0.00021	0.00023	0.00025	0.00027	0.00028
Re	0.085	0.067	0.044	0.003	0.0013

indicated that the final morphology of the droplets was less affected by the impact force and more dependent on the rheological properties (such as viscosity) of the droplets themselves, the viscosity and the ion diffusion rate of the external crosslinking solution. A low Reynolds number made the droplet deformation process more stable. Therefore, the morphologies of the resultant microgels can be precisely adjusted by regulating parameters such as the viscosities of collection solutions and crosslinking rate.

As Fe^{3+} diffused into the interior of the droplets to interact with the alginate and created an ionic crosslinking network, the crosslinking-induced deformation was likely to take place due to the uneven crosslinking across individual droplets, where the crosslinking firstly took place at the region close to the interface. This uneven crosslinking could further lead to the development of the dimple effect as a result of the synergistic effect of the viscoelastic stress of the droplet and the osmotic pressure difference between the interior of the droplet and external medium (osmolalities of the collecting solutions are calculated in Table S1†).[50] We assessed the crosslinking duration (the time period from the moment the droplet enters the collecting solutions to the moment when it starts to sink after crosslinking) in solutions with various concentrations of glycerol and $FeCl_3$. The curve in Fig. S6† showed that the degree of crosslinking changed over time and indicated that the crosslinking time exhibited a decreasing trend as the Fe^{3+} concentration increased. The crosslinking rate of the droplets was significantly influenced by the viscosity of the collection solution. A high viscosity collection solution drastically slowed down the ion diffusion rate and extended the droplets' crosslinking period. The morphological changes of the droplets were closely associated with the We, Re, and diffusion-induced crosslinking time, as demonstrated by the above experimental results. Therefore, the final morphologies of the microgels can be effectively controlled by controlling the rheological properties of the droplets, the composition of the collection liquid, and the parameters of the crosslinking kinetics.

3.3. Effect of collection solutions' viscosities and concentrations on the morphologies of Fe-alginate microgels from droplets of an aqueous solution of SA–dextran$_{500\,000}$ (2 wt%/10 wt%)

Dextran (DEX, $M_w \sim 500\,000$) is a high-molecular-weight polymer with a long molecular chain. When added to an SA solution, the dextran chains interact with the SA chains to some extent, significantly increasing the viscosity of solutions (Fig. S2†). After the addition of 10 wt% DEX 500 000 to the SA solution, the droplets (SA-DEX) exhibited a high viscosity, displaying unique deformation characteristics during the subsequent crosslinking process. Under different conditions, Fe-alginate microgels with varied morphologies were prepared by crosslinking the SA-DEX droplets in collection solutions with different concentrations of glycerol and $FeCl_3$. Specifically, the concentrations of glycerol and $FeCl_3$ in the collection solutions were varied from 0–70 wt% and 2–10 wt%, respectively. As a result, five typical morphologies of microgels, including teardrop-like, peach-like, cap-like, mushroom-like, and dimpled shapes with a large cavity (Fig. 2a), were obtained.

When the concentrations of glycerol and $FeCl_3$ were both at relatively lower levels, *i.e.*, 0–30 wt% and 2–6 wt%, teardrop-like microgels were produced. In these cases, the collection solutions had relatively low viscosities (~3.2 mPa s at the maximum). Due to the presence of Span 80, the interfacial tension between the droplet and the collection solution was reduced, which preferentially enabled the droplet to maintain a spherical shape in the droplet's production process. Upon coming into contact with Fe^{3+}, a rapid crosslinking reaction initiated, progressing from the outer layer toward the interior and forming a near-spherical bottom of teardrop-like microgels. In the early stage of deformation, the droplets were not yet fully crosslinked. However, as the density of the partially crosslinked droplets gradually increased, a downward inclination from gravity and an upward inclination from the inertial effect synergistically developed a tail at the top part of the droplet, producing a teardrop shape (Fig. S7a†).[51] When the $FeCl_3$ concentration was increased to 8 wt%, the accelerated crosslinking allowed the droplets to rapidly crosslink, preserving their deformed shape. Under these conditions, the resulting microgels exhibited a peach-like shape, indicating that the accelerated crosslinking locked the droplets at the early deformation stage (Fig. S7b†). When the glycerol concentration was raised to 70 wt% and the $FeCl_3$ concentration was in the range of 2–4 wt%, cap-like microgels with outwardly expanding concavities were produced (Fig. S7c†). Given that the droplets were dropped from a certain height, and, due to inertia, the droplets quickly came into contact with the $FeCl_3$ solution; surface tension initially dominated, and the droplets maintained their spherical shape. Meanwhile, a rapid crosslinking reaction occurred, leading to the formation of a convex gel structure at the bottom. As the surface crosslinking proceeded, the density of the droplets increased, leading to the settling of the partially crosslinked droplet. During their descent, the resistance from the viscous collecting solution caused the edges of droplets to be dragged upward. Subsequently, the droplets began to gradually float toward the oil–water interface. During this process, the top of

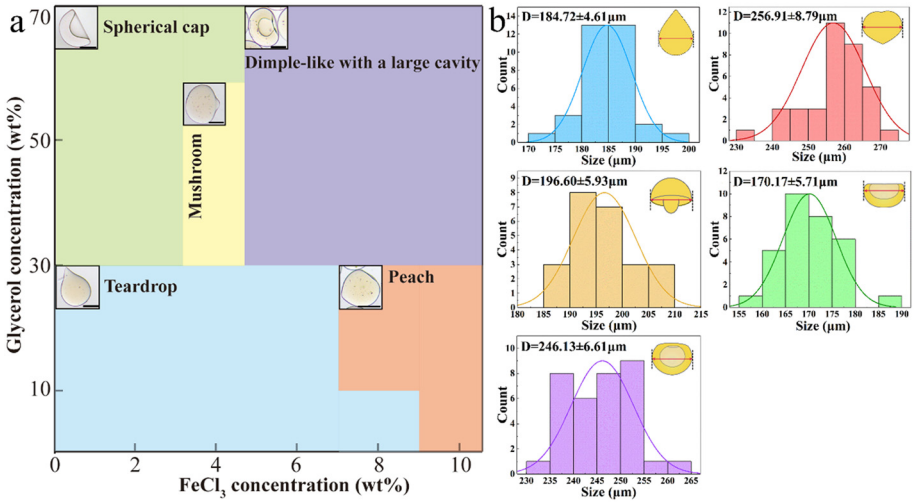

Fig. 2 a: Morphology diagram of Fe-alginate microgels generated in collection solutions with glycerol concentrations ranging from 0–70 wt% and $FeCl_3$ concentrations from 2–10 wt%, where the DP is a 2 wt% SA solution containing 10 wt% dextran. Insets provide optical microscopy images of five distinct morphologies of Fe-alginate microgel: cap-like, dimple-like with a large cavity, mushroom-like, teardrop-like, and peach-like. The scale bar for all panels denotes 100 μm. b: Particle size distribution diagrams of the five morphologies of Fe-alginate microgels.

the droplet was gradually pulled toward the center due to the uneven crosslinking between the bottom and top parts of the droplet, forming a concave shape. As the crosslinking degree further increased, the droplets gradually sank into the collecting liquid and transformed into cap-like microgels. The specific deformation process can be seen in Video S1 and Fig. S8a in the ESI.†

In the cases of collecting solutions with higher viscosity and further increased $FeCl_3$ concentrations, the resulting microgels exhibited mushroom-like or dimple-like shapes with a large cavity. The formation of mushroom-like microgels primarily resulted from the synergistic effect of the rapid crosslinking of the droplets, the inhibition of fluid diffusion by the high-viscosity collection solution, the gravity of the droplet, and shear forces from the collecting solution (Fig. S7d†). For dimple-like microgels with large cavities, the indentation differed from the outward concavity of the cap-like microgels. Instead, an inward contraction emerged (Fig. S7e†). This phenomenon was plausibly due to the high concentration of Fe^{3+}, which promoted a rapid crosslinking of the droplet's outer layer, creating a hardened shell. This rapid crosslinking locked the outer surface of the droplet at an early stage, preventing outward expansion. During the subsequent rising process, the top part of the droplet (the region experiencing the crosslinking process later than that of the bottom part) was pulled toward the center of the droplet. At this point, the diffusion rate of Fe^{3+} into the droplet decreased, resulting in a slower gelation rate at the top of the droplet, ultimately forming an inwardly concave cavity. The specific deformation process can be seen in Video S2 and Fig. S8b in the ESI.† SEM images revealed the microgel exhibited a dense and smooth surface and featured a large cavity (Fig. S9†). Overall, the final morphologies of the microgels can be effectively tuned by controlling the viscosity and the concentration of Fe^{3+} of the collection solution. This method yields microgels with uniform size across different morphologies and demonstrates excellent morphology control capabilities (Fig. 2b).

Our experimental results indicated that dimple-like Fe-Alginate microgels with large cavities exhibited a distinct deformation pattern when formed in collection solutions with high viscosities and high ion concentrations. To quantitatively analyze this deformation, we introduced a dimensionless constant, d/D, as a deformation index, where D and d represent the outer contour dimension and the cavity diameter of the microgel. By measuring and comparing d/D values, we established the correlation between microgels' morphology and changes in the compositions of the collection solutions. As shown in Fig. 3a, the viscosities of the collection solutions significantly increased with the increase in glycerol concentrations, resulting in a gradual expansion of the cavity size and, consequently, an increase in d/D values. For instance, when the concentrations of glycerol and $FeCl_3$ were set to 30 wt% and 6 wt%, the d/D value was ~0.3. The values rose to ~0.38 and 0.5, respectively, when the concentrations of glycerol were raised to 50 wt% and 70 wt% ($p < 0.001$, ANOVA). This trend suggested that the cavity diameter increased with the viscosity of the collection solution, leading to a rise in d/D values. We quantified the diffusion rate and viscous resistance by invoking the Stokes–Einstein equation:[52]

$$D_{Fe} = \frac{kT}{6\pi\eta r} \quad (3)$$

where D_{Fe} is the diffusion coefficient of Fe^{3+}, η is the solution viscosity, k is Boltzmann's constant, T is temperature, and r is the hydration radius of Fe^{3+}. The increase in glycerol concentration from 30 wt% to 70 wt% leads to the increase in η from 3.2 mPa s to 14.3 mPa s, resulting in a decrease in D_{Fe} of about 78% of its initial value. Higher glycerol

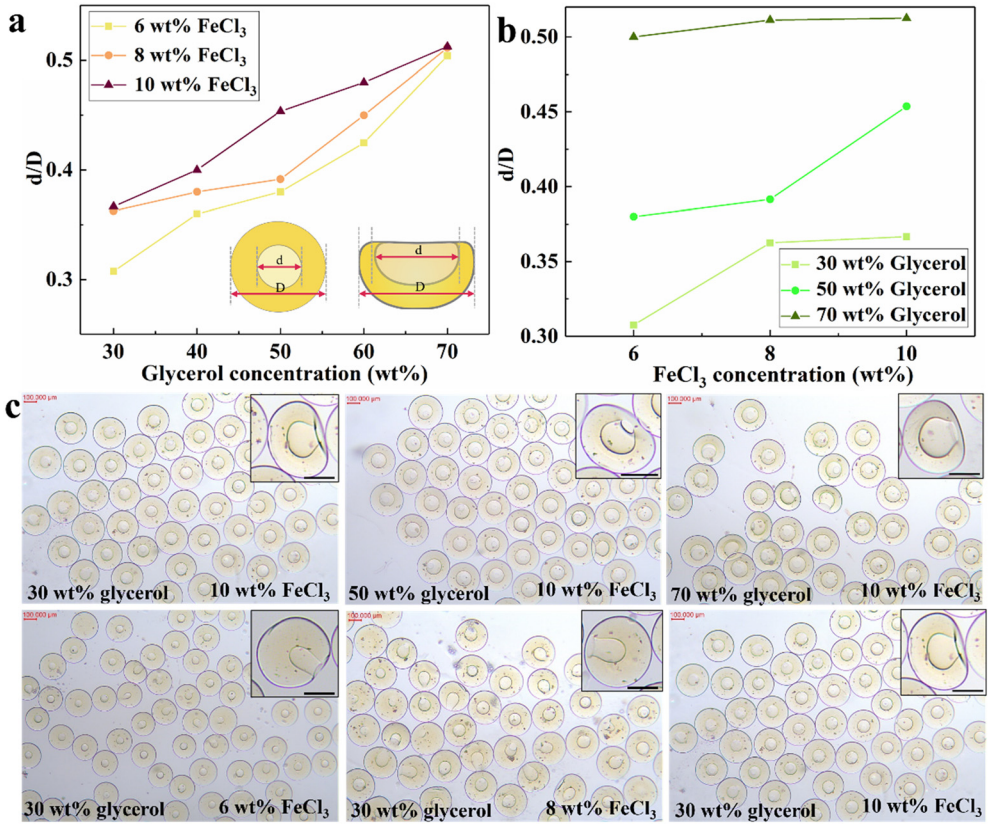

Fig. 3 a: Curves of d/D values for Fe-alginate microgels obtained in collection solutions with 4, 6, and 8 wt% of $FeCl_3$ as a function of glycerol concentrations. The inset illustrates the definitions of d and D, where d represents the maximum cavity diameter within the microgel, and D is the overall size of the microgel. b: Curves of d/D values for Fe-alginate microgels obtained in collection solutions with 30, 50, and 70 wt% glycerol as a function of $FeCl_3$ concentration. c: The first row shows optical microscopy images of Fe-alginate microgels obtained in collection solutions with a fixed 10 wt% $FeCl_3$ but a varied glycerol concentration from 30, 50, to 70 wt%, respectively. The second row shows optical microscopy images of Fe-alginate microgels obtained in collection solutions with a fixed 30 wt% glycerol and a varied $FeCl_3$ concentration from 6, 8, to 10 wt%, respectively. Data are presented as mean ± SD ($n > 30$), one-way ANOVA with Tukey's *post-hoc* test. NS: Not significant.

concentrations increased the viscosities of the collection solutions, limiting inward diffusion of Fe^{3+} and significantly enhancing the resistance during droplet sedimentation. Due to the delayed and slower crosslinking at the top of the droplet, it retained fluidity for a relatively longer period, making the top part more susceptible to being dragged inward during sedimentation. The partially crosslinked top was gradually pulled toward the center of the droplet. Meanwhile, the high-viscosity resistance further amplified this dragging effect, thereby enlarging the cavity diameter. Moreover, under varying Fe^{3+} concentrations, the d/D values exhibited a similar trend with changes in glycerol concentrations. Therefore, the cavity diameter in the microgels could be effectively controlled by adjusting the glycerol concentrations, which allowed us to precisely tune the d/D values.

Under a fixed glycerol concentration, higher Fe^{3+} concentrations generally correlated with increased d/D values. Fig. 3b illustrates this trend: the d/D value gradually rose from 0.30 to 0.367 when the concentration of $FeCl_3$ was increased from 6 wt% to 10 wt%, but the glycerol concentration was kept at 30 wt% ($p < 0.003$, ANOVA). According to Fick's Law, the diffusive flux of Fe^{3+} (J) is proportional to its concentration gradient (∇C):[53]

$$J = -D\nabla C \quad (4)$$

As the concentration of $FeCl_3$ in the collecting solution increases, and the concentration gradient of Fe^{3+} near the surface of the droplet increases, leading to an acceleration of the initial diffusion rate. However, higher Fe^{3+} concentrations accelerated the crosslinking of the droplet's outer layer, leading to the rapid formation of a gel shell. As a consequence, the diffusion of Fe^{3+} into the interior of the droplet was remarkably slowed down, leading to a slower gelation process within the inner region of the droplet. As the density of the droplet increased due to partial crosslinking, the droplet's sedimentation was accelerated, and the droplet encountered resistance from the collection solution during descent, ultimately raising the d/D value. Thus, the cavities sizes and overall morphologies of the microgels can be adjusted to a certain extent by tuning Fe^{3+} concentrations. Optical microscopy images in Fig. 3c clearly demonstrated the morphological changes of microgels under

different conditions, visually presenting the change of d/D values with concentrations of glycerol and Fe^{3+}. Furthermore, the microgels with different cavity diameters were functionalized with a solution of 0.5 wt% ruthenium-functionalized polymers to impart them with fluorescence. Through this operation, each microgel exhibited distinct and stable fluorescence, and their cavity structures were clearly visualized (Fig. S10†). The observation showed that the diameters and morphologies of the cavities were not only structurally apparent but also more distinctly visualized with fluorescent labeling. In summary, the cavity's sizes can be expanded to a certain extent by increasing the concentrations of either glycerol or Fe^{3+}, therefore raising the d/D values. This trend provided an important quantitative basis for controlling microgels' morphology, aiding in the precise structural optimization of microgels under different conditions. These findings offered valuable insights for the structural tuning of microgels for applications in payload delivery, tissue engineering, and other fields.

3.4. Effect of viscosities and Fe^{3+} concentrations of collection solutions on the morphologies of Fe-alginate microgels formed from droplets of an aqueous solution of SA–PEG_{6000} (2 wt%/10 wt%)

PEG 6000 is a non-ionic, hydrophilic polymer with low affinity to SA. Due to the neutral nature of PEG, there is a lack of strong interactions with Fe^{3+}, making it unable to participate in the crosslinking process. As a result, PEG molecules tended to be excluded from the gel network during crosslinking due to excluded volume effects, forming separate regions distinct from the rich crosslinked SA areas. This phenomenon was primarily related to the concentration-dependent behavior and conformational changes of PEG molecules. At this concentration, the hydration properties and water interaction of PEG led to thermodynamic instability in the solution, manifested as polymer–polymer repulsion and selective solute–solvent interactions. These effects further resulted in the formation of local concentration gradients, ultimately causing macroscopic phase separation.[54] Inside the droplets, the phase separation was characterized by distinct microphase structures, where the Fe–SA crosslinked network coexisted with PEG-rich regions. The specific mechanism of this separation is illustrated in Fig. 4a. This behavior also introduced unique deformation phenomena during the SA crosslinking process. Notably, significant differences in microgel morphologies in various collection solutions were also observed (Fig. 4b).

Under the conditions of low concentrations of glycerol (at 0–30 wt%) and $FeCl_3$ (2–4 wt%), the microgels exhibited a snowman-like structure with a smaller top head and a relatively larger bottom body. In this structure, the head region was noticeably darker in color than the spherical main body part. Specifically, the head region primarily consisted of PEG components that were excluded from the successful crosslinking, resulting in a darker and opaque appearance. In

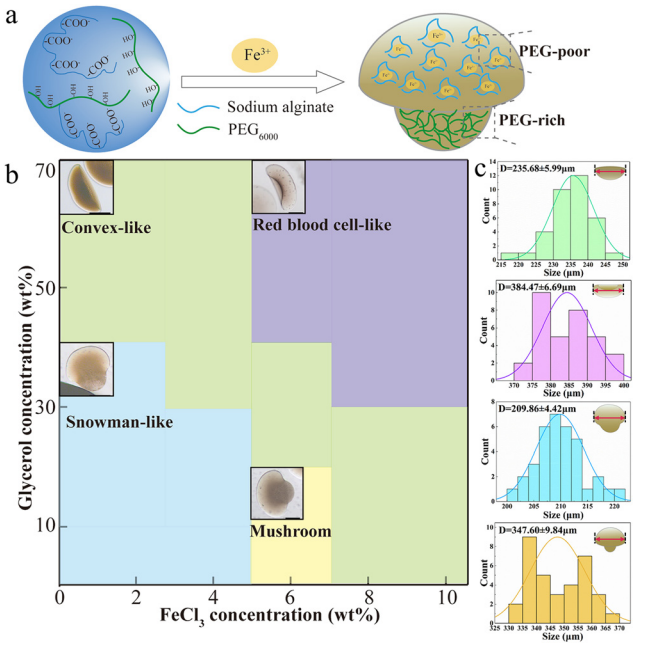

Fig. 4 a: Cartoon diagram showing the specific phase separation mechanism in Fe-alginate microgels. b: Phase diagram of Fe-alginate microgels' morphologies generated in collection solutions with glycerol concentrations ranging from 0–70 wt% and $FeCl_3$ concentrations from 2–10 wt%, where the inner phase is an aqueous solution of 2 wt% SA and 10 wt% PEG_{6000}. The insets are optical microscopy images of five different morphologies of Fe-alginate microgels: convex-like, red blood cell-like, snowman-like, and mushroom-like. The scale bar for all panels denotes 100 μm. c: Particle size distribution diagrams of the five different morphologies of Fe-alginate microgels.

contrast, the spherical main body part was lighter in color and translucent, exhibiting a translucent yellow-brown color, indicating a stable Fe-alginate gel network formed through successful crosslinking between alginate and Fe^{3+}. A noticeable color gradient existed between the PEG-rich region and the rich crosslinked Fe-alginate gel region, with a gradual transition from dark to light, as shown in the optical microscopy image (Fig. S11a†). This color gradient reflected the phase separation between PEG-rich and rich crosslinked regions. The phase separation gradually decreased with the increase in the concentrations of $FeCl_3$ (from 4 to 10 wt%). Meanwhile, the microgel's morphology also evolved into mushroom-like (Fig. S11b†) or convex-like shapes (Fig. S11c†). This change was due to the promoted crosslinking reaction between SA and Fe^{3+} under conditions of higher concentrations of Fe^{3+}. The more rapid the crosslinking, the more effective it is at trapping the PEG molecules within the droplet. This limited the migration of PEG molecules or phase separation to take place, resulting in a more uniform internal structure. The deformation process can be seen in Videos S3 and S4 and Fig. S12a and b.† Under the conditions of high concentrations of glycerol (30–70 wt%) and $FeCl_3$ (6–10 wt%), the microgels exhibited a red blood cell-like shape, with their color showing a gradient from dark to light, transitioning from the concave area to the convex region (Fig. S11d†). This can be explained by the fact that when the droplet

came in contact with the collection solution, the high concentration of Fe^{3+} led to a rapid crosslinking at the bottom of the droplet, limiting the diffusion of ions into the interior. The high-viscosity environment inhibited the upward movement of the droplet, resulting in the partially crosslinked top part of the droplet experiencing significant resistance and being dragged inward, thereby forming a concave shape.[55] The deformation process can be seen in Video S5 and Fig. S12c.† The color gradient was likely due to the differences in crosslinking rates and timeframes, which led to the uneven distribution of Fe^{3+}. The outer layer underwent an earlier and faster crosslinking, forming a more transparent and lighter-colored region. Meanwhile, the inner region of the concave area came into contact with Fe^{3+} later than the outer layer and had a relatively slower crosslinking rate, resulting in a less densely crosslinked network. Consequently, a small amount of PEG was squeezed out, making the color in the concave area darker. This color gradient reflected the occurrence of phase separation during the crosslinking process, revealing differences in structure and component distribution across different regions of the microgel. The four batches of sample microgels generated in the above collection solutions exhibited uniform particle sizes (Fig. 4c). Additionally, the microgels can be imparted with fluorescence for better morphological observations (Fig. S13†). Results showed that the fluorescence intensity of the entire gel was uniform and stable, indicating that alginate remained evenly distributed within the gel even with the occurrence of phase separation. This was because the carboxyl groups in alginate can closely bind with the positively charged groups of the ruthenium-functionalized polymers through the electrostatic attraction. From the SEM image (Fig. S14†), it can also be observed that the individual red blood cell-like Fe-alginate microgel exhibited two main parts: one was a densely crosslinked network area representing the PEG-poor region, presumed to be formed from the ionic crosslinking between SA and Fe^{3+}; the other was a relatively loose or dispersed area, likely representing the PEG-rich region. The interface between the densely crosslinked region and the PEG-rich region was clearly visible. These findings further supported the phase separation hypothesis of SA-PEG droplets during the ionic crosslinking process, providing additional insight into the distinct structures formed within the microgels. Therefore, the phase separation and the evolution of microgel morphologies indicated that the viscosities and the Fe^{3+} concentration of collection solutions

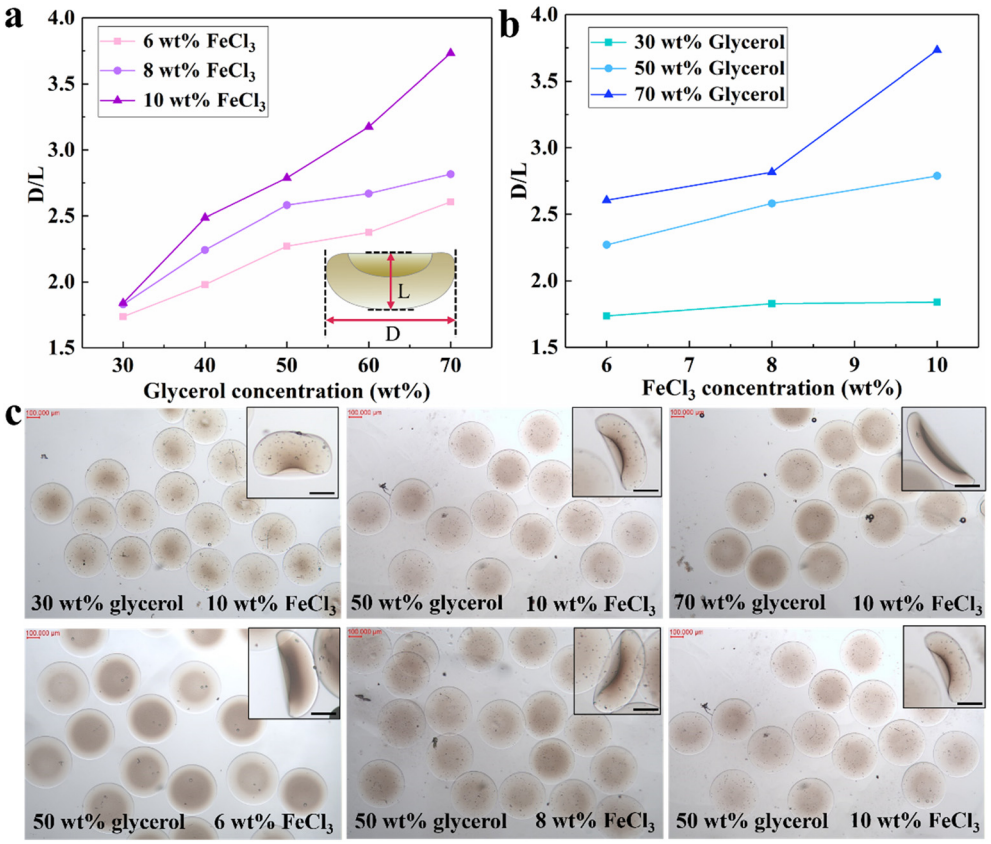

Fig. 5 a. The *D*/*L* values of Fe-alginate microgels obtained in collection solutions with 4, 6, and 8 wt% $FeCl_3$, plotted as a function of glycerol concentration. The inset defines *D* and *L*, where *D* represents the length of the microgel and *L* represents the thickness. b. The *D*/*L* ratio of Fe-alginate microgels obtained in collection solutions with 30, 50, and 70 wt% glycerol, plotted as a function of $FeCl_3$ concentration. c. The first row shows optical microscopy images of Fe-alginate microgels obtained in collection solutions with a fixed 10 wt% $FeCl_3$ and a varied glycerol concentration from 30, 50, to 70 wt%. The second row shows optical microscopy images of Fe-alginate microgels obtained in collection solutions with a fixed glycerol concentration at 50 wt% but a varied $FeCl_3$ concentration from 6, 8, to 10 wt%, respectively. Data are presented as mean ± SD ($n > 30$), one-way ANOVA with Tukey's *post-hoc* test. NS: Not significant.

played important roles in the regulation of crosslinking dynamics and material properties.

For the red blood cell-like microgels, a certain pattern in the variations of their overall size with changes in the collection solutions was observed. We defined the horizontal and vertical lengths of the microgel as D and L, respectively (as illustrated in Fig. 5a). By comparing the D/L ratio, the trend of the microgel's morphology change can be quantified. This metric helped us to quantitatively evaluate the trend of the microgel's morphology variations, especially the morphological evolution in solutions with different concentrations of glycerol and $FeCl_3$. On the one hand, the addition of glycerol primarily affected the viscosity of the droplets and the crosslinking rate. At lower concentrations of glycerol, the droplets formed gel particles with relatively smaller D and larger L. However, the viscosities of collection solutions increased with the glycerol concentration, making it harder for the droplets to be stretched in the fluid. Meanwhile, the increase in viscosities also lowered the crosslinking rate. As a result, the gradually increased D was accompanied by the gradually decreased L. Therefore, the D/L ratio showed an upward trend. As shown in Fig. 5a, when the concentrations of glycerol and $FeCl_3$ were 30 wt% and 6 wt%, respectively, the D/L value was about 1.7. The values increased to 2.3 and 2.6 when the glycerol concentration was raised to 50 wt% and 70 wt%, respectively ($p < 0.001$, ANOVA). This change was attributed to glycerol's role as a thickening agent, which slowed down the crosslinking process. Since the crosslinking reaction mainly occurred on the surface of the droplet at the initial stage, the un-crosslinked inside region, due to its high viscosity, restricted fluid movement. This generated significant resistance during the spreading process, resulting in longitudinal stretching of droplets and a decrease in thickness. Therefore, the D/L values increased with glycerol concentration. Similarly, for solutions with $FeCl_3$ concentrations at 8 wt% and 10 wt%, the D/L values also showed a consistent upward trend with an increase in glycerol concentration. On the other hand, at the same glycerol concentration, the D/L values also showed an upward trend with the increase in Fe^{3+} concentration. The concentration of Fe^{3+} played a crucial role in the crosslinking reaction, and its increase promoted the crosslinking rate, affecting the degree of gelation and morphologies of the resulting microgels. As shown in Fig. 5b, the D/L values gradually increased from 1.7 to 1.8 when the concentration of $FeCl_3$ was increased from 6 wt% to 10 wt% while maintaining the glycerol concentration at 30 wt% ($p < 0.006$, ANOVA). These trends confirmed the synergistic role of glycerol and $FeCl_3$ in enhancing the depth of the concavity. Although this change was relatively small when compared to the variations in glycerol concentrations, it still indicated that the increase in Fe^{3+} concentrations further reduced the gel thickness and increased the overall length, thereby affecting the D/L values. This trend was similar to the cases of the changes in glycerol concentration, suggesting that the increase in Fe^{3+} concentration enhanced the uniformity of the crosslinking reaction, resulting in the formation of the gel shell more rapidly. Meanwhile, the lower fluidity in the inner regions led to a similar stretching effect. These results demonstrated that the increase in either the glycerol concentration or the Fe^{3+} concentration affected the length and thickness of the resulting microgels, thereby increasing the D/L values.

The optical microscopy images in Fig. 5c show the morphological changes of the microgels under different conditions. By comparing the optical microscopy images of microgels formed in different concentrations of glycerol and $FeCl_3$, it was clear that the overall sizes and their thicknesses of the microgels, respectively, increased and decreased with the increase in the concentrations of glycerol and Fe^{3+}. This phenomenon was in close agreement with the variation trend of the D/L values, further confirming the proposed mechanism that the microgel's morphologies can be affected by the concentrations of glycerol and Fe^{3+}.

3.5. Effect of viscosities and Fe^{3+} concentration of collection solutions on the morphologies of Fe-alginate microgels formed from droplets of an aqueous solution of SA–glycerol (2 wt%/10 wt%)

Given that the above-mentioned additives were all polymers, which affected the viscoelastic properties of the DP, glycerol, which has been widely used to tune the viscosities of an aqueous solution, was also selected to serve as the additive.[56] Therefore, when an appropriate amount of glycerol was added to both the DP and the collection solution, it could be used to modulate the droplet deformation process. On the one hand, glycerol increased the viscosity of the SA solution, which helped to generate more stable droplets in the microfluidic device and control the size and shape of the droplets. Additionally, the addition of glycerol also affected the rheological properties of the droplets, enhancing their capabilities to maintain their shape in collection solutions with different concentrations of $FeCl_3$. On the other hand, glycerol can regulate the water exchange between the droplets and the collection solution. Due to its contribution to osmolality, glycerol decelerated the diffusion of water from the droplets into the collection solutions with high concentrations of $FeCl_3$, influencing the rate of droplet shrinkage and the final morphology of microgels. Therefore, the osmotic effect and the variations in $FeCl_3$ concentration collectively influenced the deformation process of the microgels.

Fig. 6a shows the morphology phase diagram of Fe-alginate microgels formed from SA–glycerol (2 wt%/10 wt%) droplets that were collected in solutions with varied concentrations of glycerol (0–70 wt%) and $FeCl_3$ (2–10 wt%). Four different morphologies, including mushroom-like, red blood cell-like, pointed-tailed mushroom-like, and convex-like, were observed. The mushroom-like microgel with a pointed tail appeared in collection solutions with relatively low viscosities (0–30 wt% glycerol) and low Fe^{3+} concentrations (2–4 wt% $FeCl_3$) (as shown in Fig. S15a†). The formation mechanism of this structure can

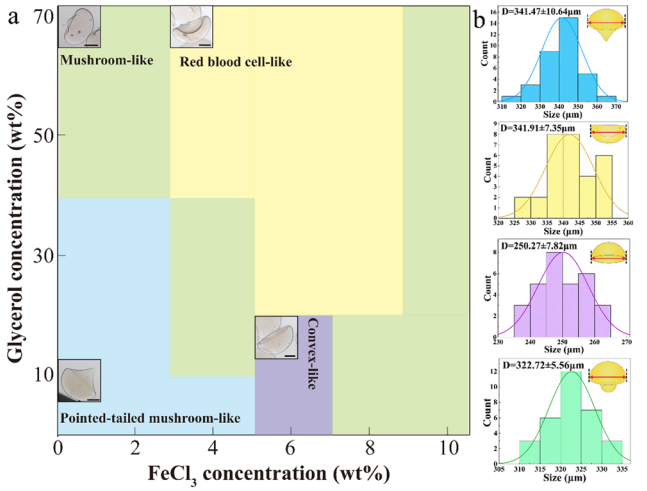

Fig. 6 a: Morphological phase diagram of Fe-alginate microgels formed in collection solutions with glycerol concentrations ranging from 0 to 70 wt% and $FeCl_3$ concentrations ranging from 2 to 10 wt%. The inner phase is an aqueous solution of 2 wt% SA and 10 wt% glycerol. The inset figures are optical microscopy images of five different morphologies of the Fe-alginate microgels: pointed-tailed mushroom-like, red blood cell-like, mushroom-like, and convex-like. The scale bar for all panels denotes 100 μm. b: Particle size distribution diagrams of the four morphologies of the Fe-alginate microgels.

be explained from the perspective of the temporal nature of the crosslinking and the diffusion characteristics of Fe^{3+}. In collecting solutions with low viscosities, *i.e.* 3 mPa s, Fe^{3+} was allowed to diffuse to the droplets' surface at a relatively higher rate and initiated crosslinking with SA. This led the bottom region of the droplet to crosslink first and form a relatively stable crosslinked shell, while the top part of the droplets remained under fluidic state. Because of the relatively low concentration of Fe^{3+} in the collection solution, fewer ions were diffused into the interior of droplets and they could not penetrate the entire droplet uniformly within a short timeframe. The lower amount of Fe^{3+} inside the droplet was localized, resulting in relatively weaker crosslinking at the top region. Consequently, the uneven crosslinking between the top and bottom parts of the droplet allowed the top part to stretch and deform downward under the influence of surface tension and gravity during the crosslinking process, eventually forming a 'tail' structure. As time progresses, the top region became surrounded by external Fe^{3+} and began to crosslink, solidifying the 'tail' shape. The deformation process can be seen in Video S6 and Fig. S16a in the ESI.† When the $FeCl_3$ concentration was increased to 6 wt%, the microgel gradually displayed a convex shape in solutions with low glycerol concentrations (0–10 wt%). It can be concluded that the increase in Fe^{3+} concentration led to more uniform crosslinking. The low-viscosity environment facilitated the rapid diffusion of Fe^{3+}, allowing for synchronous crosslinking of the entire droplet and maintaining a smooth surface. The balance between gravity and surface tension further favored the deformation of the droplet into a hemispherical form, resulting in stable convex-like microgels (Fig. S15b†). In the cases of solutions with high viscosities (30–70 wt% glycerol), when the Fe^{3+} concentration was at a low level (2 wt% $FeCl_3$), the shape of the microgel tended to be mushroom-like (Fig. S15c†). In this case, the high glycerol concentration increased the viscosity of the collection solution to 14.3 mPa s, slowing down the diffusion of Fe^{3+} towards the droplet. The slow crosslinking allowed Fe^{3+} to initially crosslink the bottom region and outer surface of the droplet, forming a crosslinked shell and creating the 'mushroom cap' structure. Due to the localization of an insufficient amount of Fe^{3+}, the top region remained more fluidic. The crosslinking at the bottom part then stretched the un-crosslinked top region downwards. The bottom crosslinked shell supported the droplet, while the top part got elongated, forming the 'stem' of the mushroom shape. This structure reflected the prioritization of external crosslinking, while the top part formed fewer crosslinks due to diffusion limitations. The deformation process can be seen in Video S7 and Fig. S16b in the ESI.† When the $FeCl_3$ concentration was further raised to 8 wt%, the red blood cell-like microgel emerged in collection solutions with relatively higher viscosities (30–70 wt% glycerol) (as shown in Fig. S15d†). The formation of this morphology was mainly due to the faster and more uniform crosslinking caused by the higher Fe^{3+}. Meanwhile, the high-viscosity environment limited the migration speed of the droplet and the diffusion rate of the ions, causing the top of the droplet to be gradually pulled toward the center during the rising process, resulting in the formation of a concave morphology. The deformation process can be seen in Video S8 and Fig. S16c in the ESI.† These two morphologies were the most common during the entire process. Interestingly, when the $FeCl_3$ concentration reached 10 wt%, the microgel consistently formed a mushroom shape, regardless of the glycerol concentration (0–70 wt%). This suggested that, after reaching a certain concentration, $FeCl_3$ became the dominant factor that controls the crosslinking process. At this point, the rapid and uniform distribution of Fe^{3+} and the strong crosslinking effect led to the formation of mushroom-like structures, regardless of the external environment. Fig. 6b shows that the produced microgels maintain their particle sizes within a certain range and a concentrated size distribution. Specifically, the diameters of these microgels are uniform, with a small standard deviation, which ensured their consistency and reliability in subsequent applications. The SEM images showed that the surface of the microgel was relatively smooth, and the overall structure was robust, indicating a uniform ionic crosslinking process that formed a dense network structure (Fig. S17†). By exploring the mechanisms behind the morphological changes, we can provide the theoretical support and experimental basis for the morphological control and functionalization design of microgels.

In collection solutions with high viscosities (glycerol concentrations at 50–70 wt%) and high ion concentrations ($FeCl_3$ concentrations at 6–8 wt%), red blood cell-like microgels exhibited a distinct morphological evolution pattern. To quantify the morphology evolution trend, we defined the overall length from the horizontal direction and the vertical concave depth of the microgel as D and L,

respectively. The *D*/*L* value was used to evaluate the trend in morphological changes, where a smaller *D*/*L* value indicated a greater degree of concavity. As shown in Fig. 7a, the *D*/*L* value gradually decreased with increased glycerol concentrations in the collection solutions, reflecting an enhanced concavity of the microgels. For instance, when the concentrations of glycerol and $FeCl_3$ were at 30 wt% and 6 wt%, respectively, the *D*/*L* value was ~9.2. When the concentration of glycerol was raised to 50 wt% and 70 wt%, the *D*/*L* values correspondingly decreased to approximately 6.1 and 5, respectively. This indicated that the concavity of the microgels deepened with the increase in glycerol concentration, as evidenced by the relative increase in the concave depth *L*, leading to a reduction in the *D*/*L* values. A similar trend was observed when the $FeCl_3$ concentration was increased to 8 wt%, where the *D*/*L* value decreased from 8.3 to 4.1 with the increase in glycerol's concentration. The concentration of Fe^{3+} also significantly influenced the degree of concavity. Under a fixed glycerol concentration, the *D*/*L* values decreased with the increase in the concentration of $FeCl_3$, indicating that the concavity became more pronounced as the concentration of Fe^{3+} increased (Fig. 7b). For example, in the collection solution containing 50 wt% glycerol, when the concentration of $FeCl_3$ was increased from 4 wt% to 8 wt%, the *D*/*L* values decreased from 6.4 to 5 ($p < 0.005$, ANOVA). These experimental results demonstrated that higher concentrations of glycerol and $FeCl_3$ led to microgels with deeper concavities, resulting in reduced *D*/*L* values. Fig. 7c shows optical microscopy images of the changes in the microgel's concavity under different concentrations of glycerol and $FeCl_3$. The images clearly showed that with an increase in the concentrations of glycerol and $FeCl_3$, the depth of the concavity in the microgels progressively increased. This trend aligned with the observed *D*/*L* variations, demonstrating that the concavities of microgels can be effectively controlled by adjusting the concentrations of glycerol and $FeCl_3$. This allows for precise tuning of microgel's morphologies under various conditions.

To verify the universality of the deformation mechanism proposed in this study, we further applied the strategy to the chitosan/tripolyphosphate (CS-TPP) microgel system and investigated the impact of the collecting solutions' viscosity

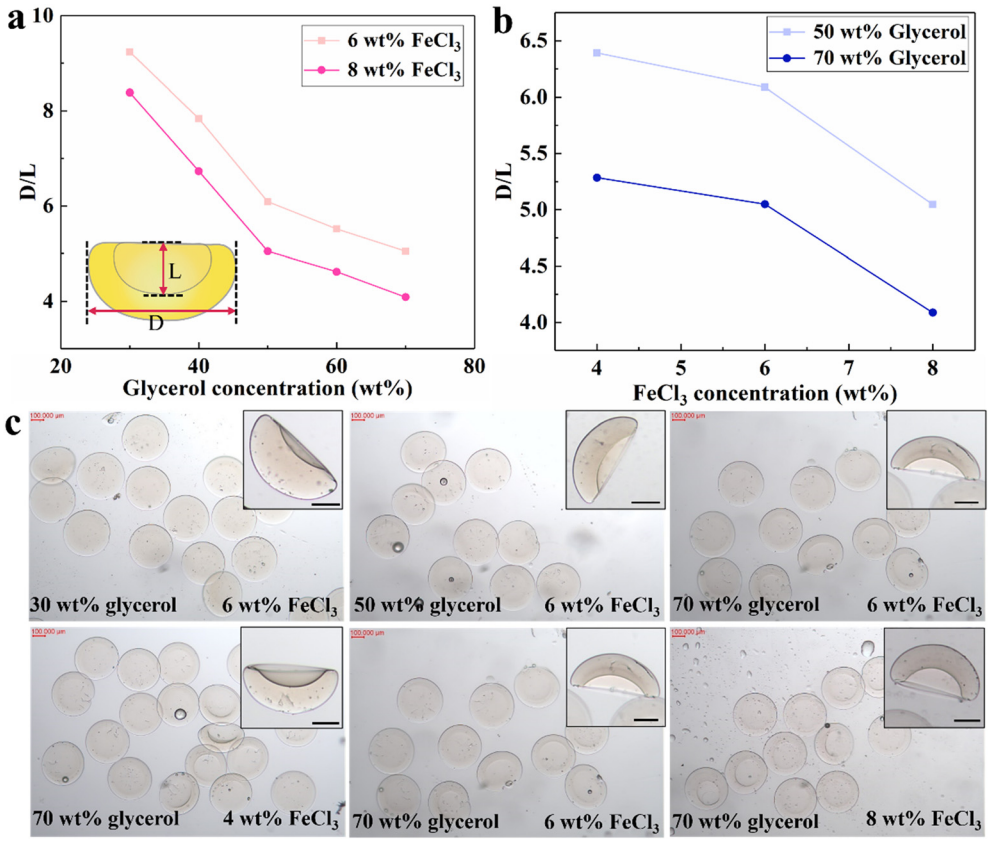

Fig. 7 a. Variation curves of the *D*/*L* values of Fe-alginate microgels formed in collection solutions containing 6 wt% or 8 wt% $FeCl_3$ but with varied concentrations of glycerol. The inset cartoon figure defines *D* and *L*, where *D* represents the horizontal length of the microgel, and *L* indicates the vertical depth of the concave region. b. Variation curves of the *D*/*L* values of Fe-alginate microgels formed in collection solutions with 50 wt% and 70 wt% glycerol as a function of $FeCl_3$ concentration. c. The first row presents optical microscopy images of Fe-alginate microgels formed in collection solutions with a fixed concentration of $FeCl_3$ (6 wt%) but varied concentrations of glycerol from 30 wt%, 50 wt%, to 70 wt%. Alternatively, the second row are optical microscopy images of Fe-alginate microgels formed in collection solutions with a fixed concentration of glycerol (70 wt%) but varied concentrations of $FeCl_3$ from 4 wt%, 6 wt%, to 8 wt%. Data are presented as mean ± SD ($n > 30$), one-way ANOVA with Tukey's *post-hoc* test. NS: Not significant.

(regulated by the glycerol concentration) and the crosslinker concentration (TPP content) on the morphologies of the resultant microgels. Experimental results showed that when the glycerol concentration in the collection solution was fixed at 10 wt% with increased TPP concentration (from 2 to 6 wt%), the horizontal projected diameter (D) of the CS-TPP microgels increased from 350 ± 8 μm to 433 ± 6 μm, while the longitudinal thickness (L) decreased from 144 ± 6 μm to 124 ± 5 μm (Fig. S18a–c†). Similarly, when the TPP concentration in the collection solution was fixed at 6 wt% while the concentration of glycerol was varied from 10 to 50 wt%, the D and L of the CS-TPP microgels respectively increased from 433 ± 5 μm to 486 ± 6 μm and decreased from 126 ± 6 μm to 92 ± 5 μm (Fig. S18d–f†). It is worth noting that we also observed changes in the shape of the microgels by altering the viscosity of the chitosan droplets. Specifically, as the viscosity of the droplets increased, the D and L of the microgels increased from 304 ± 5 μm to 520 ± 6 μm and decreased from 200 ± 8 μm to 108 ± 5 μm, respectively (Fig. S19†). The evolution trends of these morphological parameters are highly consistent with the variation rules of the D/L values observed in the Fe-alginate system (Fig. 5), indicating that the synergistic effect of the crosslinking rate and the viscosity of droplets also dominates the morphological evolution of the CS-TPP microgels. Through the comparative study of the two systems, we have revealed the common rules of the morphological evolution of microgels formed from the ionic crosslinking method. The discovery of this mechanism not only deepens the understanding of the microgel formation kinetics but also provides a theoretical framework for expanding the morphological regulation of other crosslinking systems.

3.6. Comparative study of payload release profiles of spherical and dimpled Fe-alginate microgels

With their three-dimensional network structure, high water content and excellent biocompatibility, hydrogels have shown great potential in biomedical fields such as drug delivery and tissue regeneration.[57–59] To investigate the regulatory mechanism of morphological engineering strategies on the model molecule's release performance of Fe-alginate

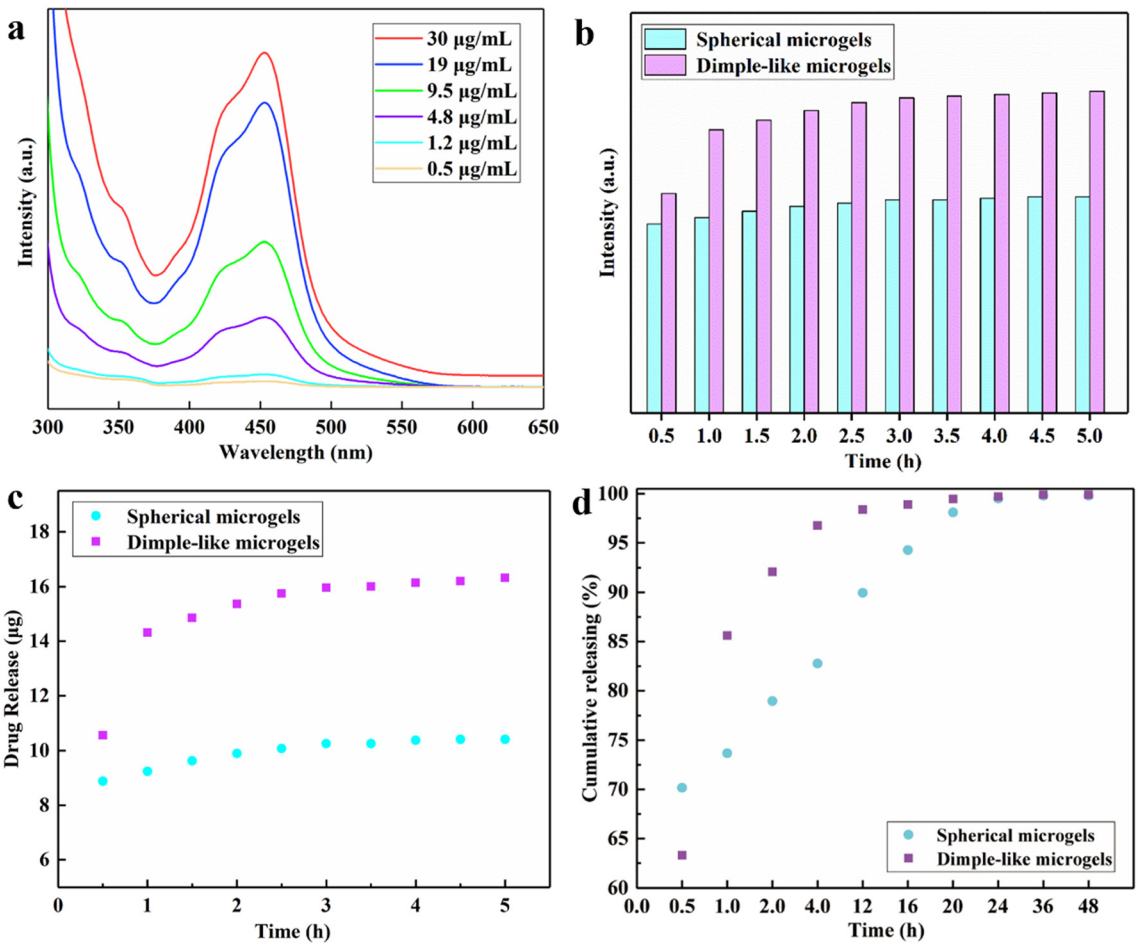

Fig. 8 a. The UV-vis absorption spectra of model molecules at different concentrations. b. The bar chart presenting the UV absorption intensity of model molecule release from spherical microgels and dimple-like microgels between 0.5 and 5 hours of monitoring. c. The dynamic changes in molecule release amounts of the two microgels with different morphologies within 5 hours. d. The cumulative relative release rates of the two microgels with different morphologies within 48 hours.

microgels and their biomedical application potential, this study employed concave-structured microgels (D-MG) and spherical microgels (S-MG) as model systems. The structural stability and payload release behavior differences of these two morphological microgels were systematically evaluated under a simulated physiological environment (PBS buffer, pH 7.00 ± 0.02). $Ru(bpy)_3Cl_2{\cdot}6H_2O$ was used as a model molecule, which was loaded into the negatively charged Fe-alginate gel network *via* electrostatic interaction. Ultraviolet-visible (UV-vis) spectroscopy analysis (Fig. 8a) revealed that $Ru(bpy)_3^{2+}$ exhibited a strong absorption peak at 454 nm, which corresponds to its characteristic metal–ligand charge transfer (MLCT) effect, with its peak intensity showing a linear correlation with payload concentration (R^2 = 0.998), providing a foundation for quantitative analysis. Fluorescence microscopy imaging (Fig. S20†) further confirmed that both microgels could effectively load model molecules.

We summarized the UV absorption spectral intensity and cumulative payload release amounts of the two morphological microgels as show in Fig. 8b and c. Model molecule release kinetic studies showed that both microgels achieved maximum release rates in the initial release phase (0–0.5 h). Specifically, D-MGs reached 21.12 μg h^{-1}, 19% higher than S-MGs (17.76 μg h^{-1}). The absorbance value of D-MGs (0.137) was 1.16-fold greater than that of S-MGs (0.118) ($p < 0.001$), resulting in a noticeable higher cumulative payload release from D-MGs (8.88 μg) compared to S-MGs (10.56 μg). This phenomenon was attributed to the unique concave structure of D-MGs, which increased the specific surface area and provided more payload adsorption sites, thereby significantly enhancing payload loading capacity. During the intermediate release phase (0.5–2 h), the release rate of spherical microgels dropped sharply to an average of 0.68 μg h^{-1}. In contrast, concave microgels maintained high release rates (0.5–1 h: 7.5 μg h^{-1}), decreasing to 1 μg h^{-1} between 1–2 h but still 1.47 times higher than that of the S-MGs. This behavior may be closely related to the localized payload storage sites within the concave structure. After 2 h, both microgels exhibited significantly reduced release rates (D-MGs: 0.18 μg h^{-1}; S-MGs: 0.3 μg h^{-1}), but their cumulative release percentages diverged remarkably (Fig. 8d). D-MGs achieved 92% of total payload release (approximately 15.36 μg) by 2 h and nearly completed release by 5 h, whereas S-MG only released 79% (9.9 μg) of total payload at this time and required ~24 h to achieve near complete release. Notably, the 24 h cumulative release of S-MGs was equivalent to the amount released by D-MGs within 10 minutes (Fig. S21†).

These results highlight the unique advantages of D-MGs in rapid payload delivery, making them particularly suitable for applications requiring rapid attainment of therapeutic concentrations (*e.g.*, antibacterial dressings, emergency medications) and stable long-term payload delivery (*e.g.*, hormone replacement therapy, chronic disease management). Although the microgels were not applied to biological experiments, this study provided novel insights into the design of novel delivery systems based on morphological engineering strategies. Based on the study of the payload release behaviors, we systematically evaluated the structural stability and long-term preservation properties of payload microgels. The payload microgels maintained their structural integrity throughout the extended release process of up to 48 h, with no obvious wrinkling or disintegration of the surface morphology (Fig. S22†). This excellent structural integrity ensured the controlled release of model molecules by diffusion rather than sudden release through carrier disintegration, confirming the reliability of the microgel as a payload carrier.

4. Conclusion

This study systematically investigated the influence of compositions of droplets and collection solutions on the morphological control of Fe-alginate microgels. By addition of additives with different molecular weights (dextran, PEG, and glycerol) to the SA solutions, the viscosities of the DP were successfully adjusted, which remarkably affected the droplets' sizes and deformation under shear forces during microfluidics-induced droplet formation. The results indicated that the rheological properties of the DP played a key role in determining the initial droplets' morphology and subsequent crosslinking dynamics. The combination of glycerol and Fe^{3+} in the collection solution further enabled precise control over the microgel's morphologies. By adjusting the concentrations of glycerol and $FeCl_3$, various structured microgels, including teardrop, mushroom, hemispherical, and concave shapes, were successfully fabricated. The thickening and osmotic effects of glycerol, as well as the Fe^{3+} concentration's control over the crosslinking rate, were key factors driving morphological transitions. Experimental results have shown that the higher concentrations of glycerol and Fe^{3+} in the collecting solutions resulted in deeper concavities of the formed microgels and more distinct morphological features. Compared with many existing studies that relied solely on a single parameter to regulate the morphology of microgels, the present study innovatively revealed the dynamic interaction mechanism between droplet composition and external cross-linking conditions. This systematic regulation strategy not only broke through the limitations of traditional methods in terms of morphological diversity and controllability, but also provided a standardized evaluation system for microgel morphology regulation through the quantitative analysis of D/L and d/D values. The cross-system validation using the chitosan/tripolyphosphate (CS-TPP) microgel system further confirmed the universality of the proposed deformation mechanism and established a theoretical framework for the morphological control of different crosslinking systems. Payload release experiments highlighted D-MGs with an accelerated release profile, offering advantages for on-demand delivery. Although systematic tests on the

in vitro biocompatibility and *in vivo* performance of the microgels prepared in this study have not been conducted, their high monodispersity, morphological stability, and potential for functional design exhibit broad application prospects in fields such as drug delivery, tissue engineering, and optical materials.

Data availability

The datasets generated and analyzed during the current study are available from the corresponding author upon reasonable request. Specific experimental data, raw characterization results, and ESI† are included in the article and its supporting files. Additional information or customized data processing scripts used in this study can also be provided upon request for academic and non-commercial purposes.

Conflicts of interest

The authors declare that they have no known competing financial interests or personal relationships that could have appeared to influence the work reported in this paper.

Acknowledgements

This work is supported by the Fundamental Research Funds for the Central Universities (No. 2023JBMC021 (Y. H.), No. 2024YJS196 (J. C.)). Y. H. is also grateful for the open research funds support from Guangdong Provincial Key Laboratory of Technique and Equipment for Macromolecular Advanced Manufacturing (No. 20240518), the fund from Hubei Provincial Key Laboratory of Green Materials for Light Industry, Hubei University of Technology (No. 202409B01), and Fund of Key Laboratory of Advanced Materials of Ministry of Education (Tsinghua University) No. Advmat-2402.

References

1 D. Huang, J. Wang, M. Nie and Y. Zhao, *Adv. Mater.*, 2023, **35**, 2301192.
2 K. Matsumiya, N. F. Inagaki and T. Ito, *Langmuir*, 2024, **40**, 1247–1256.
3 L. C. Cai, G. Wang and Y. Zhao, *Research*, 2021, **2021**, 9895674.
4 C. Li, J. Wang and Y. Wang, *Acta Pharm. Sin. B*, 2019, **9**, 1145–1162.
5 D. M. Roquero and K. Evgeny, *Sens. Actuators Rep.*, 2022, **4**, 100095.
6 A. C. Daly, L. Riley and T. Segura, *Nat. Rev. Mater.*, 2020, **5**, 20–43.
7 S. N. Asadi and A. Z. Doyle, *Soft Matter*, 2022, **18**, 6848–6856.
8 D. Wang, S. Maharjan and X. Kuang, *Sci. Adv.*, 2022, **8**, 6900.
9 X. R. Deng, Y. Hou and L. Jiang, *Lab Chip*, 2021, **21**, 1517–1526.
10 H. Zhou, L. Xu and Y. Wen, *J. Colloid Interface Sci.*, 2017, **490**, 233–241.
11 C. Yang, Y. Yu and Y. Zhao, *Research*, 2023, **6**, 0034.
12 D. K. Hwang, D. Dendukuri and P. S. Doyle, *Lab Chip*, 2008, **8**, 1640–1647.
13 J. A. Champion and S. Mitragotri, *Proc. Natl. Acad. Sci. U. S. A.*, 2006, **103**, 4930–4934.
14 S. Tan, Y. J. Yin and X. C. Xue, *Adv. Funct. Mater.*, 2023, **33**, 2305071.
15 S. H. Mashiyama, R. Sato and T. Kato, *Lab Chip*, 2024, **24**, 171–181.
16 Y. L. Wang and J. Hu, *Carbohydr. Polym.*, 2021, **269**, 118262.
17 Y. Z. Wang, D. G. Zhang and H. Shang, *NPG Asia Mater.*, 2022, **14**, 1–9.
18 Y. Liu, J. Li and T. Wu, *Sens. Actuators, B*, 2024, **418**, 136331.
19 Y. Liu, Z. Chen and J. H. Xu, *Green Chem. Eng.*, 2024, **5**, 16–30.
20 J. Li, N. Li and B. Liu, *Int. J. Bioprint.*, 2024, **10**, 1951.
21 D. Nishit, S. Z. Alisar and B. Srijanani, *Proc. Natl. Acad. Sci. U. S. A.*, 2009, **106**, 21495–21499.
22 D. An, A. Warning and K. G. Yancey, *Nat. Commun.*, 2016, **7**, 12401.
23 Y. Yang, S. I. Vagin and B. Rieger, *Macromol. Rapid Commun.*, 2024, **45**, e2300721.
24 Z. Meng, W. Wang and R. Xie, *Lab Chip*, 2016, **16**, 2673–2681.
25 J. A. Champion, Y. K. Katare and M. Samir, *Proc. Natl. Acad. Sci. U. S. A.*, 2007, **104**, 11901–11904.
26 S. K. Suh, K. Yuet and D. K. Hwang, *J. Am. Chem. Soc.*, 2012, **134**, 7337–7343.
27 C. Liu, P. L. Plata and M. Zaroudi, *ACS Appl. Bio Mater.*, 2020, **3**, 7357–7362.
28 Z. Luo, L. Sun and F. Bian, *Adv. Sci.*, 2023, **10**, e2206150.
29 S. Daradmare, H. Son and C. S. Lee, *Langmuir*, 2023, **39**, 13876–13889.
30 C. C. Zhou, Y. Liu and C. X. Guo, *Mater. Today*, 2023, **67**, 178–202.
31 N. G. Min, B. Kim and T. Y. Lee, *Langmuir*, 2015, **31**, 937–943.
32 S. Lee, J. Rutte and R. Dimatteo, *ACS Nano*, 2022, **16**, 38–49.
33 X. M. Liu, H. Wang and T. Sun, *Institute of Electrical and Electronics Engineers/Robotics Society of Japan*, 2015, pp. 798–803.
34 K. Feng, N. Gao and W. Zhang, *Small*, 2020, **16**, e1903884.
35 Y. Liu, T. Naotomo and T. Nisisako, *Sens. Actuators, B*, 2019, **283**, 802–809.
36 E. Y. Liu, S. Jiang and D. A. Weitz, *Lab Chip*, 2018, **18**, 323–334.
37 X. He and L. Chu, *Chemical Industry Engineering Progress*, 2019, **38**, 4109.
38 C. Zhou, J. Man and J. Li, *Ceram. Int.*, 2022, **48**, 27590–27596.
39 Y. Gao, C. Zhao and F. Sainsbury, *J. Colloid Interface Sci.*, 2021, **584**, 528–538.
40 Y. Hu, Q. Wang and Y. Yang, *Biomicrofluidics*, 2012, **6**, 026502.
41 A. J. D. Kruger, O. Bakirman, L. P. B. Guerzoni and A. Jans, *Adv. Mater.*, 2019, **31**, e1903668.
42 S. J. Shin, J. Y. Park and J. Y. Lee, *Langmuir*, 2007, **23**, 9104–9108.

43 Y. Hu, G. Azadi and A. M. Ardekani, *Carbohydr. Polym.*, 2015, **120**, 38–45.
44 P. Plata, Y. Liu and L. C. Nitsche, *Phys. Rev. Fluids*, 2018, **3**, 093601.
45 C. Zhang, R. Grossier and N. Candoni, *Biomater. Res.*, 2021, **25**, 1–26.
46 D. M. Roquero, A. Othman and A. Melman, *Mater. Adv.*, 2022, **3**, 1849–1873.
47 J. Chen, H. Shen and Y. Heng, *Macromol. Rapid Commun.*, 2024, **45**, 2400084.
48 M. Hsiao, S. Lichter and L. G. Quintero, *Phys. Fluids*, 1988, **31**, 3560–3562.
49 P. B. S. Lissaman, *Annu. Rev. Fluid Mech.*, 1983, **15**, 223–239.
50 S. Mukherjee and K. Sarkar, *Phys. Fluids*, 2011, **23**, 1.
51 C. J. Martinez, J. W. Kim and Y. C. Ortiz, *Macromol. Biosci.*, 2012, **12**, 946–951.
52 C. C. Miller and J. Walker, The Stokes-Einstein law for diffusion in solution, *Proc. R. Soc. London, Ser. A*, 1924, **106**, 724–749.
53 J. Crank, *The mathematics of diffusion*, Oxford university press, 1979.
54 S. Di Fonzo, B. Bellich and A. Gamini, *Polymer*, 2019, **175**, 57–64.
55 E. Q. Li, D. Beilharz and S. T. Thoroddsen, *Phys. Rev. Fluids*, 2017, **2**, 073602.
56 Y. Hu, S. Wang and A. Abbaspourrad, *Langmuir*, 2015, **31**, 1885–1891.
57 J. Yao, H. Fu and Y. Q. Xia, *Adv. Funct. Mater.*, 2025, 2504004.
58 S. H. Yang, X. Zhang and Y. M. Tan, *Langmuir*, 2025, **41**, 4498–4511.
59 H. T. Liu, Y. Q. Wang and H. Wang, *Adv. Sci.*, 2020, **7**, 1903739.